Experimental and density functional study of Mn doped Bi_2Te_3 topological insulator

A. Ghasemi, D. Kepaptsoglou, A. I. Figueroa, G. A. Naydenov, P. J. Hasnip, M. I. J. Probert, Q. Ramasse, G. van der Laan, T. Hesjedal, and V. K. Lazarov

Citation: APL Materials **4**, 126103 (2016); doi: 10.1063/1.4971354
View online: http://dx.doi.org/10.1063/1.4971354
View Table of Contents: http://aip.scitation.org/toc/apm/4/12
Published by the American Institute of Physics

Experimental and density functional study of Mn doped Bi_2Te_3 topological insulator

A. Ghasemi,[1] D. Kepaptsoglou,[2] A. I. Figueroa,[3] G. A. Naydenov,[1] P. J. Hasnip,[1] M. I. J. Probert,[1] Q. Ramasse,[2] G. van der Laan,[3] T. Hesjedal,[4] and V. K. Lazarov[1,a]

[1]*Department of Physics, University of York, York YO10 5DD, United Kingdom*
[2]*SuperSTEM Laboratory, SciTech Daresbury Campus, Daresbury WA4 4AD, United Kingdom*
[3]*Magnetic Spectroscopy Group, Diamond Light Source, Didcot OX11 0DE, United Kingdom*
[4]*Department of Physics, Clarendon Laboratory, University of Oxford, Oxford OX1 3PU, United Kingdom*

(Received 20 August 2016; accepted 15 November 2016; published online 15 December 2016)

We present a nanoscale structural and density functional study of the Mn doped 3D topological insulator Bi_2Te_3. X-ray absorption near edge structure shows that Mn has valency of nominally 2+. Extended x-ray absorption fine structure spectroscopy in combination with electron energy loss spectroscopy (EELS) shows that Mn is a substitutional dopant of Bi and Te and also resides in the van der Waals gap between the quintuple layers of Bi_2Te_3. Combination of aberration-corrected scanning transmission electron microscopy and EELS shows that Mn substitution of Te occurs in film regions with increased Mn concentration. First-principles calculations show that the Mn dopants favor octahedral sites and are ferromagnetically coupled. [http://dx.doi.org/10.1063/1.4971354]

Three-dimensional topological insulators (3D TIs) are a new class of materials with promising properties both for exploring fundamental physics and developing novel technological applications as spintronic devices.[1] TIs are insulating in their bulk. However, their surface states are gapless and protected by time-reversal symmetry (TRS) which makes them immune to backscattering from disorder and non-magnetic impurities.[2,3] The combination of magnetism with TIs can lead to a number of interesting phenomena, such as the point-charge-induced magnetic monopole and topological contributions to the Faraday and Kerr magneto-optical effects.[3] Most importantly, the interplay between topologically protected surface states and ferromagnetism is expected to give rise to different and unconventional spintronic effects, potentially leading to device applications.[4]

A typical representative of a 3D TI is Bi_2Te_3, a narrow-gap semiconductor with an indirect band gap of 160 meV at 300 K. The unit cell of Bi_2Te_3 is composed of three weakly bonded Te–Bi–Te–Bi–Te quintuple layers (QLs) with a hexagonal crystal structure.[5] However, Bi_2Te_3 exhibits no magnetic ordering, and single crystals are typically *p*-type semiconductors that can become superconducting under pressure.[6] In order to induce magnetic ordering in Bi_2Se_3 or Bi_2Te_3, doping with transition metals is an established route.[5,7] Upon doping with magnetic elements, TRS can be broken and the Dirac electrons can become effectively massive.[8] According to first-principles calculations, this is the case when TIs are doped with V, Cr, Mn, or Fe, which can break TRS and open a band gap in the surface band structure.[9] Even though long-range ferromagnetic order has been reported at low temperatures in materials such as Cr-doped Bi_2Se_3,[3,10] Mn- and Fe-doped Bi_2Se_3,[11,12] and Bi_2Te_3,[13] the correlation between the local chemical environment of magnetic dopant and magnetic order is not well understood. Indeed, direct correlation between the magnetic dopants concentration and functional properties of TIs could be rather challenging, for example, doping with Mn in many host materials results in structural or chemical inhomogeneities affecting the magnetic properties.[11]

[a]Author to whom correspondence should be addressed. Electronic mail: Vlado.lazarov@york.ac.uk

The main goal of achieving room-temperature ferromagnetism in homogeneously doped 3D TIs has therefore proven difficult to achieve.[14] Although Mn doped Bi_2Te_3 crystals and thin films with doping concentrations of up to 10% were found to be ferromagnetic with Curie temperatures of around 10 K,[15] it is not clear if ferromagnetism is due to secondary, undesirable Mn-containing phases or the homogeneous doping of Mn into the Bi_2Te_3 matrix, i.e., as a substitutional dopant. Due to the layered crystal structure of these materials, several possible lattice sites exist for the incorporation of magnetic dopants. These include substitutional incorporation on Bi or Te sites within the QLs, as well as interstitial incorporation within the QLs, and the incorporation in the van der Waals gap between the QLs.[15] In these ternary systems, it is of great importance to preserve the overall bulk electronic properties upon doping, and, moreover, to reduce the defect densities in general.

In this work, we show that the low Mn doping concentrations (~2.5 at.%) in the Bi_2Te_3 preserved the structural integrity of the thin film. By using real space atomic imaging and X-ray spectroscopy, we show that even at this low doping concentrations Mn is substitutionally incorporated into Bi_2Te_3, as well as in the van der Waals gap. First-principle calculations performed for a number of Mn configurations as a substitutional and interstitial dopant show that ferromagnetic ordering is favored. At higher doping concentrations (e.g., ~6 at.%), secondary phases appear and the crystallinity of the matrix is significantly deteriorated. This work shows that inducing long-range ferromagnetic order by Mn doping Bi_2Te_3 can be achieved even at low concentrations, independent of the local chemical environment.

The Mn doped Bi_2Te_3 thin films were grown by molecular beam epitaxy (MBE) on *c*-plane sapphire substrates. Prior to growth, the samples were solvent-cleaned and baked in the load-lock for 8 h. First, a Bi_2Te_3 buffer layer was deposited at a substrate temperature of 200 °C. The doped layers were then grown with a Mn doping concentration ranging from ~2% to 9%, measured with an *in situ* beam-flux monitor (BFM), and given in % with respect to the Bi flux, at a substrate temperature of 250 °C. Standard effusion cells were used for the co-deposition of Bi, Mn, and Te. All evaporation materials used were of 99.9999% purity and the films were deposited in a Te-rich environment to reduce the formation of Bi-Te anti-site defects and Te vacancies. Growing with a Bi:Te flux ratio of 1:10, the deposition rate is Bi-limited at ~0.4 nm min^{-1}. Nominal Mn-doping concentrations were adjusted using the Mn:Bi flux ratio, as measured by the BFM.

The film quality was evaluated using *in situ* reflection high-energy electron diffraction (RHEED, not shown) and *ex situ* X-ray diffraction (XRD). Judging from the film peaks observed in the out-of-plane XRD spectra, depicted in Figure 1(d), the 2.5% Bi_2Te_3 film is rhombohedral, *c*-axis oriented, and free of peaks from secondary phases.

Cross-sectional transmission electron microscopy (TEM) specimen preparation was done by focused ion beam (FIB) methods using a FEI Nova 200 NanoLab high-resolution field emission gun scanning electron microscope. A protective layer of C was thermally evaporated onto the film surface outside of the FIB chamber; two further sacrificial layers of Pt were deposited by the electron and ion beams to protect the film from Ga-ion implantation and damage.

Structural characterization scanning transmission electron microscopy (STEM) imaging and EEL spectroscopy measurements were performed in a Nion UltraSTEM100^{TM} equipped with a Gatan Enfina spectrometer. The microscope was operated at 100 kV, with a convergence angle of 30 mrad; at these optical conditions the electron probe size is determined to be ~0.9 Å. The inner detector angle for high-angle annular dark field (HAADF)-STEM imaging was 76 mrad. The native energy spread of the electron beam for EELS measurements was 0.3 eV, with the spectrometer dispersion set at 0.3 and 1 eV/channel, depending on the required energy range. The EELS collection angle was 31 mrad. For enhancing the contrast of the atomically resolved spectra, a noise-reduction routine was applied using principal component analysis (CiMe-plugin for Gatan's Digital Micrograph 2.3 software suite).[16] Due to the overlap of the Te $M_{4,5}$ and Mn $L_{2,3}$ core loss edges (and O *K* at the interface), elemental maps were created by multiple linear least squares (MLLS) fitting[17] or reference spectra, after background subtraction using a power law. The fitting was performed using the routine built in Gatan's Digital Micrograph software suite and reference Te $M_{4,5}$ and Mn $L_{2,3}$ edges (available

in the Gatan EELS atlas) and where applicable the O *K* edge (acquired from the Al_2O_3 substrate) as fitting components, respectively.

X-ray absorption near edge structure (XANES) and extended X-ray absorption fine structure (EXAFS) spectra were collected at room temperature at the Mn *K* edges of Mn doped Bi_2Te_3. A Mn foil and powdered MnO, Mn_2O_3, and MnTe compounds were measured as reference. The powdered standards were pressed into pellets with the optimized quantity for measurements in the transmission mode. A nine-element Ge fluorescence detector was used to measure the thin films, with the beam at grazing incidence (<5°) with respect to the sample plane. All spectra were acquired in quick-EXAFS mode with monochromatic beam from the Si(111) crystals. The energy range for each scan allowed us to extract information in the extended region up to k = 12 Å^{-1}. EXAFS spectra were processed and analyzed using different tools of the IFFEFIT XAFS package.[18] Fits of the EXAFS signal were performed on the *R* space in a range from 1.5 to 3.2 Å using a sinusoidal window function, so that it covered Mn in the first coordination shell. The parameters fitted were the interatomic distance (R), the Debye-Waller factor (σ^2) for each scattering path, and a general shift in the threshold energy (ΔE_0). The amplitude reduction factor $S_0{}^2$ was set to that obtained for the fit of the MnTe standard ($S_0{}^2 = 0.71$). Data analysis and fitting on all references and samples were performed in ARTEMIS, making use of models based on crystallographic information obtained from the inorganic crystal structure database. The atomic clusters used to generate the scattering paths for fitting were generated with ATOMS.[19]

Structure optimization, total-energy and electronic-structure calculations were performed from first-principles using the plane-wave density functional theory (DFT) program CASTEP[20] with the generalized gradient approximation (GGA) of Perdew-Burke-Ernzerhof (PBE)[21] for the exchange-correlation functional. Ultrasoft pseudopotentials were used for each element, with a 500 eV plane-wave cutoff energy. Internal atomic positions were fully optimized until the force on each atom is ≤0.05 eV Å^{-1} and the total energy converges within 0.02 meV/atom. The Brillouin zone was sampled using a Monkhorst-Pack[22] **k**-mesh of 5 × 5 × 1 for bulk Bi_2Te_3 and a **k**-mesh of 3 × 3 × 1 for all 2 × 2 × 1 supercell systems with Mn. Hexagonal lattice constants for bulk Bi_2Te_3 (a = 4.43 Å and c = 30.53 Å) were also calculated from first-principles. Semi empirical dispersion correction (SEDC)[23] is included to account for the weak van der Waals interactions between Bi_2Te_3 quintuple layers. All calculations were taking spin polarization into account. Spin-orbit coupling was not included as initial tests showed that it does not play an important role with respect to relative energy differences between different configurations.

Figure 1(a) shows a cross-sectional overview of a $Mn_xBi_{2-x}Te_3$ thin film grown on *c*-plane Al_2O_3 by MBE. The atomic number dependence ($\sim Z^{1.8}$) of the HAADF contrast clearly outlines the

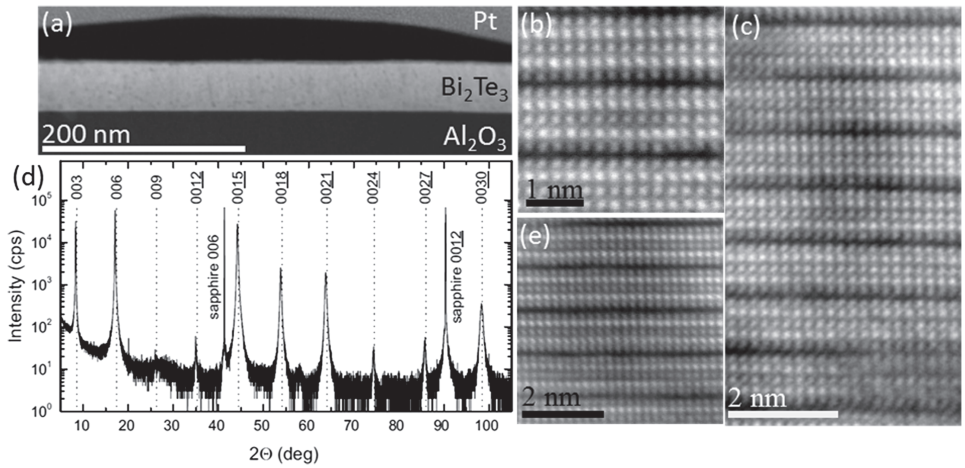

FIG. 1. (a) Low magnification HAADF-STEM image of the Bi_2Te_3 film on Al_2O_3 (0001) substrate. ((b), (c), and (e)) Atomically resolved HAADF-STEM images of different places of the Bi_2Te_3 film. A good crystalline quintuple layer structure of the Bi_2Te_3 film is present. (d) X-Ray diffraction diagram showing both film and substrate peaks as labelled.

Bi_2Te_3 film and the Al_2O_3 substrate. The film has uniform thickness with a good crystallinity. Atomic resolution HAADF imaging (Figures 1(b), 1(c)), and (1(e)) shows the good structural ordering of the film, with distinctive QL repeat unit in different regions. The abrupt change in the HAADF image contrast between the substrate and film indicates a chemically abrupt substrate-film interface, while the white fringes are showing the continuous QL structure of the film. The XRD further shows the single crystalline nature of the grown films on a larger scale (Figure 1(d)).

The presence of transition-metal (TM) and rare-earth dopants in the grown film, as well as their chemical state, can be studied by XANES,[24] hence we employed this technique to reveal the Mn chemical environment in the grown films. Figure 2(a) shows the normalized XANES spectra at the Mn *K* edge of the doped Bi_2Te_3 thin film. Comparison of the energy position of the absorption jump for the thin film with the references of the relevant standard compounds suggests that the Mn dopants in Bi_2Te_3 have a valence state close to that of the MnTe, implying 2+. These results are in good agreement with TM dopants, such as Cr, Mn, and Fe, in Bi_2Se_3 topological insulator thin films determined by x-ray absorption spectroscopy and x-ray magnetic circular dichroism at the TM $L_{2,3}$ and *K* edges.[12,25,26]

The local ordering structure of the Mn doped Bi_2Te_3 thin film can be studied from the $\chi(k)$ EXAFS signal through a Fourier transform (FT) analysis, shown in Figure 2(b), performed over a *k* range of 2.5–10.5 $Å^{-1}$ using a k^2 weight, a $\Delta k = 1$ $Å^{-1}$, and a sinusoidal window function. The best fits of the FT magnitude, $|\chi(R)|$ (Figure 2(b) and the real part of its inverse FT, Re $|\chi(q)|$, in Figure 2(c)) were achieved with Mn in an octahedral environment of Te (and Se) atoms. We note that the presence of Se in the samples was due to the unintentional Se doping during growth in the Se–Te MBE system. Results of other fit attempts can be found in the supplementary material (see Figures S1–S3 as well as Tables S1–S3). The values of the structural parameters obtained from the fit are listed in Table I, together with the nominal coordination and bonding of Bi atoms in Bi_2Te_3 and Bi_2Se_3. Comparison of Mn–Te and Mn–Se distances with Bi–Te and Bi–Se of the undoped structure (Table I) shows a strong local contraction of the bonds, which has been observed in similar TM-doped structures.[12,25] The σ^2 values are high in all cases, which can be understood as a high dispersion of bond distances and an increasing structural disorder in the crystal with incorporation of Mn, suggesting that Mn neighbourhood is rather heterogeneous. Oxidation effects might also play a role in the structural disorder, as observed for Fe dopants in Bi_2Se_3[12] and rare-earth dopants in Bi_2Te_3.[24] However, the

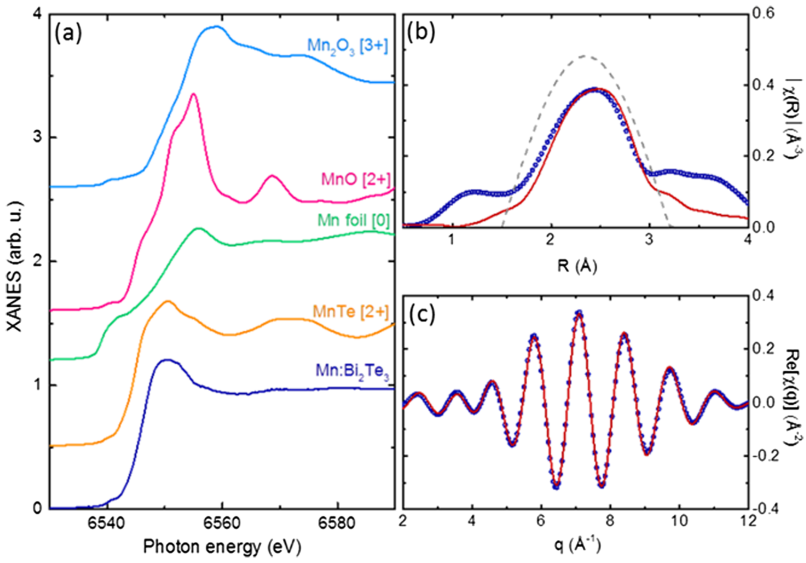

FIG. 2. (a) Mn *K* edge XANES for a Mn doped Bi_2Te_3 thin film and comparison with MnTe, MnO, and Mn_2O_3 powder samples, and Mn foil for reference. The Mn oxidation state is indicated in square brackets. The spectra have been offset vertically for clarity. (b) Fourier transform of the EXAFS signal at the Mn *K* edge on the thin film (symbols) together with the best fit to the first coordination shell (solid curve). The dashed curve shows the sine window function. (c) Contribution of the first coordination shell to the EXAFS signal (symbols) together with its best fit (solid curve).

TABLE I. Structural parameters obtained from Mn *K* edge EXAFS fits for the Mn doped Bi_2Te_3 thin film shown in Figure 2(b). Nominal coordination and bonds of Bi_2Te_3 and Bi_2Se_3 according to the crystallographic information in ICSD database are listed for comparison. Coordination number, *N*, interatomic distance, *R*, and Debye-Waller factor, σ^2, for each path are shown. A value of $\Delta E_0 = (3.3 \pm 0.9)$ eV was obtained from the fit.

Mn:Bi_2Te_3	Mn–Te1	Mn–Te2	Mn–Se
N	1.5	1.5	3
R (Å)	2.93 ± 0.02	3.07 ± 0.02	2.70 ± 0.02
σ^2 (Å^2)	0.026 ± 0.005	0.026 ± 0.005	0.009 ± 0.005
Bi_2Te_3	Bi–Te_1	Bi–Te_2	...
N	3	3	...
R (Å)	3.033	3.248	...
Bi_2Se_3	Bi–Se_1	Bi–Se_2	...
N	3	3	...
R (Å)	2.952	3.021	...

extracted contributions of MnTe, MnSe, and Mn_2O_3 from the linear combination fit of the XANES region show that the electronic structure of the Mn doped Bi_2Te_3 is more similar to the MnTe than the oxides (see Figure S4 and Table S4 of the supplementary material). These results point to Mn dopants incorporating heterogeneously, both as a substitutional and interstitial dopant in the van der Waals gap within the structure. Hence, the varied bonding environment rather than at well-defined crystallographic positions.

Next we focus on determining the spatial distribution of the Mn dopants on a nanoscale in the Bi_2Te_3 film. Direct imaging of Mn dopants in atomic resolution by Z-contrast in the HAADF images is particularly challenging due to the low *Z* of Mn ($Z_{Mn} = 25$) in comparison to Bi ($Z_{Bi} = 83$) and Te ($Z_{Te} = 52$), as well as the low concentration of Mn in the film. In order to get an unambiguous signature of the Mn spatial distribution in the film on a nanometer scale, we employed spatially resolved STEM-EELS measurements. A large field-of-view HAADF-STEM image of the film in cross section shows the characteristic QL structure of the Bi_2Te_3 film, Figure 3(a). At closer inspection, it can be seen that the HAADF image intensity of the film is not uniform; patches of lower intensity (dark patches) can be observed throughout, indicating a compositional variation across the film, possibly due to a non-uniform distribution of the Mn dopants. In order to test this hypothesis, EELS elemental mapping has been performed, as marked by a brown rectangle in Figure 3(a) and enlarged in Figure 3(b). Simultaneous acquisition of EELS has been used to produce elemental maps of Mn and Te shown in Figures 3(c) and 3(d). The elemental maps show that Mn is present throughout the film (Figure 3(c)), although its distribution is not uniform. In fact, the observed dark patches in the HAADF images

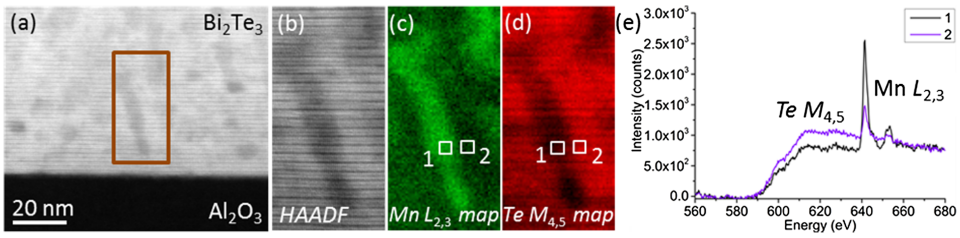

FIG. 3. (a) HAADF-STEM survey image from the Bi_2Te_3. (b) HAADF-STEM signal from the region of interest outlined in (a), produced simultaneously with the EELS acquisition. (c) Mn $L_{2,3}$ EELS signal showing higher concentration of Mn in the dark patch areas visible in (b). (d) Te $M_{4,5}$ EELS signal showing a distribution anti-correlated to that of Mn. (e) Background-subtracted Mn $L_{2,3}$ and Te $M_{4,5}$ edges obtained from the grain-boundary and off-boundary regions labelled as 1 and 2 in (c) and (d), showing enhanced Mn signal and decreased Te signal at the grain boundary.

correlate directly with the regions of higher Mn presence, confirming that the observed dark patches have increased Mn concentration, compared to the rest of the film. Moreover, comparing the Te elemental map (Figure 3(d)) to Mn and the HAADF signals (Figures 3(c) and 3(b), and extracted spectra in Figure 3(e)), one finds that the dark regions in HAADF have a lower Te concentration (see also Figure S5 of the supplementary material). The decrease of the Te signal in these areas (and relative increase in Mn content) while clearly retaining the ordered atomic structure of the QLs suggests that in regions with increased Mn concentration Mn also substitutes Te– in addition to the predicted more energetically favorable Bi atomic positions, as has been reported previously.[27] A similar analysis in the interface region is shown in Figure S6 of the supplementary material, which also indicates the Mn segregation at the interface within 1 nm region. As for the presence of oxygen in the EELS map (Figure S6 of the supplementary material), the EELS measurements were performed on thin foils, which have been exposed to air for some time before observation in the electron microscope, and therefore the presence of some degree of surface oxidation cannot be avoided. The results from STEM-EELS confirm the EXAFS results showing that the local environment of the Mn atoms in the Bi_2Te_3 thin film is heterogeneous. The large variability in measured Mn–Te distances, as shown in Table I, is consistent with Mn incorporating substitutionally on Bi sites but also as interstitials in the van der Waals gap.

In order to shed light on the atomic coordination sites of the Mn presence in the Bi_2Te_3 film, as well as for understanding the magnetic ordering in the material due to incorporation of Mn in the possible substitutional and interstitial sites, we performed first-principle calculations. On a $2 \times 2 \times 1$ supercell, we investigate the energetic and magnetic ordering of the preferred site of the Mn in the van der Waals gap, Bi, and Te substitutions. For this purpose, 16 different configurations have been considered, as the two Mn atoms can occupy multiple sites in the van der Waals gap as well as in the same or in different QLs.

First we show the results for the Mn residing in the van der Waals gap. Figure 4(a) shows the typical QLs bulk-structure of Bi_2Te_3. Figure 4(b) shows the model of the energetically most favorable configuration of the Mn atom residing in the interstitial sites, i.e., the octahedral ($B–B_1$) sites. Total-energy calculations found that Mn on the B site is by 0.19 eV energetically more favorable than the tetrahedral (A) site. In all considered configurations of Mn in the van der Waals gap, the preferred Mn position remains on the octahedral B sites, Figure S7 of the supplementary material. These

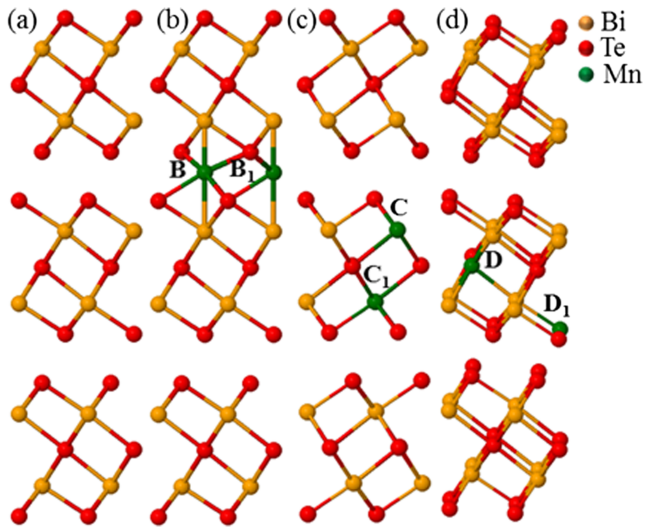

FIG. 4. The most energetically favorable configurations for Mn occupying the available interstitial and substitutional sites. (a) shows the quintuple layer structure of Bi_2Te_3 with no Mn dopant. (b) shows the most favorable configuration when Mn dopants octahedrally occupy the van der Waals gap (B and B_1). (c) The most favorable configuration when Mn atoms substitute the closest Bi sites in two different Bi planes (C and C_1). (d) shows the energetically favorable position when Mn dopants occupy the furthest Te sites in two nearby Te planes (D and D_1). The model has been tilted for clarity. Bi, Te, and Mn atoms are represented by yellow, red, and green spheres, respectively.

TABLE II. The final magnetic moments for the most energetically favorable configurations of Mn dopants in the Bi_2Te_3 structure. The labels ((b), (c), and (d)) refer to the illustrations in Figure 4.

Model	Mn position	Magnetic moments (μ_B)
(b) $B–B_1$	van der Waals gap	+4.10 and +4.10
(c) $C–C_1$	Bi substitution	+4.44 and +4.41
(d) $D–D_1$	Te substitution	–5.04 and –5.11

calculations are consistent with the EXAFS results presented above. In addition, the calculations show that Mn atoms prefer to stay in the same van der Waals gap rather than move to the next gap. All considered configurations and magnetic moments are presented in Figure S7 and Table S4 of the supplementary material.

Next we consider the energetics of Mn dopants occupying Bi and Te substitutional sites. Figures 4(c) and 4(d) show the most favorable configurations of Mn dopants occupying Bi and Te atomic sites, respectively. For Bi substitution, most favorable configuration is when Mn atoms occupy the closest Bi sites in two different Bi planes denoted as C and C_1, Figure 4(c). In the case of Te substitution (Figure 4(d)), Mn atoms are most energetically stable when they occupy the furthest Te sites in the same QL, the D and D_1 sites. All the considered configurations and energetics of magnetic ordering (i.e., antiferromagnetic versus ferromagnetic) are presented in Figures S8 and S9, and Tables S5 and S6 of the supplementary material. For all of the configurations presented above, energetically favor the ferromagnetic ordering with values of the magnetic moment shown in Table II. These results show that for considered atomic configurations, independent of the Mn occupation site, Mn dopants will tend to be ferromagnetically ordered in Bi_2Te_3 films.

Finally we show that films with increased Mn doping concentration (~6 at.%) have significant change in their atomic structure and local chemistry, Figure S10 of the supplementary material. In these films, the QL structure of Bi_2Te_3 is deteriorated and presences of secondary phases, rich in Mn, are observed. Hence the benefit of Mn dopants for magnetic 3D TIs based on Bi_2Te_3 is limited to lower Mn dopant concentrations.

In summary, we presented a structural study of Mn doped Bi_2Te_3 thin films on Al_2O_3 (0001) substrates. Structural and spectroscopic analysis using aberration-corrected STEM-EELS and EXAFS has shown that Mn dopants in Bi_2Te_3 film tend to accumulate in the van der Waals gap as well as enter the lattice substitutionally on Bi sites. In addition, Mn can also substitute Te in regions of very high Mn concentration. Structural optimizations and energy calculations suggest that octahedral sites are the most favorable positions for Mn occupation in the van der Waals gap. Furthermore, they showed that the closest Bi sites in different planes and furthest Te sites in nearby planes are most favorable configurations for Mn occupying Bi and Te sites, respectively. The DFT calculations for Mn atoms occupying all the different possible sites predict ferromagnetic coupling. This study shows that at low concentrations (e.g., ~2.5 at.%), Mn can be readily incorporated as a dopant in Bi_2Te_3 thin films, fully preserving the crystal structure of Bi_2Te_3 without inducing secondary phases, and hence presents a system with promising properties as a magnetic 3D TI.

See supplementary material for additional high magnification HAADF-STEM images, EXAFS fittings, EELS data, DFT calculation results for all considered configurations, and HAADF-STEM images of Mn doped Bi_2Te_3 with higher doping percentage (~6 at.%).

This publication arises from research funded by the John Fell Oxford University Press Research Fund. We acknowledge Diamond Light Source for time on B18 under proposal SP-9178 and access to the Surface and Interface Laboratory for AFM and XRD experiments, and RCaH for their hospitality. We thank L. Collins-McIntyre for help with the MBE growth. The SuperSTEM Laboratory is the U.K. National Facility for Aberration-Corrected STEM, supported by the Engineering and Physical Sciences Research Council (EPSRC). V.K.L. acknowledges financial support from EPSRC, Grant No. EP/K03278X/1. All data created during this research are available by request from the University of York Data Catalogue https://dx.doi.org/10.15124/14dfd1eb-0080-4e05-80a8-c605447dcb82.

[1] J. Henk, A. Ernst, S. V. Eremeev, E. V. Chulkov, I. V. Maznichenko, and I. Mertig, Phys. Rev. Lett. **108**, 206801 (2012).
[2] J. E. Moore, Nature **464**, 194 (2010).
[3] P. P. J. Haazen, J.-B. Laloë, T. J. Nummy, H. J. M. Swagten, P. Jarillo-Herrero, D. Heiman, and J. S. Moodera, Appl. Phys. Lett. **100**, 2404 (2012).
[4] L. He, X. Kou, and K. L. Wang, Phys. Status Solidi RRL **7**, 50 (2013).
[5] J. M. Zhang, W. Zhu, Y. Zhang, D. Xiao, and Y. Yao, Phys. Rev. Lett. **109**, 266405 (2012).
[6] J. L. Zhang, S. J. Zhang, H. M. Weng, W. Zhang, L. X. Yang, Q. Q. Liu, S. M. Feng, X. C. Wang, R. C. Yu, L. Z. Cao, L. Wang, W. G. Yang, H. Z. Liu, W. Y. Zhao, S. C. Zhang, X. Dai, Z. Fang, and C. Q. Jin, Proc. Natl. Acad. Sci. U. S. A. **108**, 24 (2011).
[7] A. Ghasemi, D. Kepaptsoglou, L. J. Collins-McIntyre, Q. Ramasse, T. Hesjedal, and V. K. Lazarov, Sci. Rep. **6**, 26549 (2016).
[8] X. F. Kou, W. J. Jiang, M. R. Lang, F. X. Xiu, L. He, Y. Wang, Y. Wang, X. X. Yu, A. V. Fedorov, P. Zhang, and K. L. Wang, J. Appl. Phys. **112**, 063912 (2012).
[9] J. M. Zhang, W. Ming, Z. Huang, G. B. Liu, X. Kou, Y. Fan, K. L. Wang, and Y. Yao, Phys. Rev. B **88**, 235131 (2013).
[10] L. J. Collins-McIntyre, S. E. Harrison, P. Schönherr, N.-J. Steinke, C. J. Kinane, T. R. Charlton, D. Alba-Veneroa, A. Pushp, A. J. Kellock, S. S. P. Parkin, J. S. Harris, S. Langridge, G. van der Laan, and T. Hesjedal, Europhys. Lett. **107**, 57009 (2014).
[11] M. D. Watson, L. J. Collins-McIntyre, L. R. Shelford, A. I. Coldea, D. Prabhakaran, S. C. Speller, T. Mousavi, C. R. M. Grovenor, Z. Salman, S. R. Giblin, G. van der Laan, and T. Hesjedal, New J. Phys. **15**, 103016 (2013).
[12] A. I. Figueroa, G. van der Laan, L. J. Collins-McIntyre, G. Cibin, A. J. Dent, and T. Hesjedal, J. Phys. Chem. C **119**, 17344 (2015).
[13] J. Choi, S. Choi, J. Choi, Y. Park, H. M. Park, H. W. Lee, B. C. Woo, and S. Cho, Phys. Status Solidi B **241**, 1541 (2004).
[14] C. Niu, Y. Dai, M. Guo, W. Wei, Y. Ma, and B. Huang, Appl. Phys. Lett. **98**, 252502 (2011).
[15] J. Růžička, O. Caha, V. Holý, H. Steiner, V. Volobuiev, A. Ney, G. Bauer, T. Duchoň, K. Veltruská, I. Khalakhan, V. Matolín, E. F. Schwier, H. Iwasawa, K. Shimada, and G. Springholz, New J. Phys. **17**, 013028 (2015).
[16] G. Lucas, P. Burdet, M. Cantoni, and C. Hébert, Micron **52–53**, 49 (2013).
[17] R. F. Egerton, *Electron Energy-Loss Spectroscopy in the Electron Microscope,* 3rd ed. (Springer, 2011), p. 490.
[18] B. Ravel and M. Newville, J. Synchrotron Radiat. **12**, 537 (2005).
[19] B. Ravel, J. Synchrotron Radiat. **8**, 314 (2001).
[20] S. J. Clark, M. D. Segall, C. J. Pickard, P. J. Hasnip, M. I. J. Probert, K. Refson, and M. C. Payne, Cryst. Mater. **220**, 567 (2005).
[21] J. P. Perdew, K. Burke, and M. Ernzerhof, Phys. Rev. Lett. **77**, 3865 (1996).
[22] H. J. Monkhorst and J. D. Pack, Phys. Rev. B **13**, 5188 (1976).
[23] E. R. McNellis, J. Meyer, and K. Reuter, Phys. Rev. B **80**, 205414 (2009).
[24] A. I. Figueroa, G. van der Laan, S. E. Harrison, G. Cibin, and T. Hesjedal, Sci. Rep. **6**, 22935 (2016).
[25] A. I. Figueroa, G. van der Laan, L. J. Collins-McIntyre, S. L. Zhang, A. A. Baker, S. E. Harrison, P. Schönherr, G. Cibin, and T. Hesjedal, Phys. Rev. B **90**, 134402 (2014).
[26] L. J. Collins-McIntyre, M. D. Watson, A. A. Baker, S. L. Zhang, A. I. Coldea, S. E. Harrison, A. Pushp, A. J. Kellock, S. S. P. Parkin, G. van der Laan, and T. Hesjedal, AIP Adv. **4**, 127136 (2014).
[27] Y. S. Hor, P. Roushan, H. Beidenkopf, J. Seo, D. Qu, J. G. Checkelsky, L. A. Wray, D. Hsieh, Y. Xia, S. Y. Xu, D. Qian, M. Z. Hasan, N. P. Ong, A. Yazdani, and R. J. Cava, Phys. Rev. B **81**, 195203 (2010).